

## Article

# Fingerprint-Based Localization Enabled by Low-Rank Matrix Reconstruction in Intelligent Reflective Surface-Assisted Networks

Shiru Duan <sup>1</sup>, Yuexia Zhang <sup>2,3,\*</sup> and Ruiqi Liu <sup>4</sup>

- <sup>1</sup> Key Laboratory of Information and Communication Systems, Ministry of Information Industry, Beijing Information Science and Technology University, Beijing 100101, China; shiru.duan@bistu.edu.cn
- <sup>2</sup> Key Laboratory of Modern Measurement & Control Technology, Ministry of Education, Beijing Information Science & Technology University, Beijing 100101, China
- <sup>3</sup> Beijing Key Laboratory of High Dynamic Navigation Technology, Beijing Information Science and Technology University, Beijing 100101, China
- <sup>4</sup> Wireless and Computing Research Institute, ZTE Corporation, Beijing 100029, China
- \* Correspondence: zhangyuexia@bistu.edu.cn

**Abstract:** The intelligent reflective surface (IRS) is a novel network node that consists of a large-scale passive reflective array to obtain a customized reflected wave direction by modulating the amplitude phase, which can be easily deployed to change the wireless signal propagation environment and enhance the communication performance under a non-line-of-sight (NLOS) environment, where location services cannot perform accurately. In this study, a low-rank matrix reconstruction-enabled fingerprint-based localization algorithm for IRS-assisted networks is proposed. Firstly, a 5G positioning system based on IRSs is constructed using multiple IRSs deployed to reflect signals. This enables the base station to overcome the influence of NLOS and receive the positioning signal of the point to be positioned. Then, the angular domain power expectation matrix of the received signal is extracted as a fingerprint to form a partial fingerprint database. Next, the complete fingerprint database is reconstructed using the low-rank matrix fitting algorithm, thereby considerably reducing the workload of building the fingerprint database. Finally, maximal ratio combining is used to increase the gap between the fingerprint data, and the Weighted K-Nearest Neighbor (WKNN) algorithm is used to match the fingerprint data and estimate the location of the points to be located. The simulation results demonstrate the feasibility of the proposed method to achieve sub-meter accuracy in an NLOS environment.

**Keywords:** 5G; 6G; intelligent reflective surface; localization; fingerprint; matrix completion



**Citation:** Duan, S.; Zhang, Y.; Liu, R. Fingerprint-Based Localization Enabled by Low-Rank Matrix Reconstruction in Intelligent Reflective Surface-Assisted Networks. *Electronics* **2024**, *13*, 1743. <https://doi.org/10.3390/electronics13091743>

Academic Editor: Arturo de la Escalera Hueso

Received: 19 March 2024  
Revised: 24 April 2024  
Accepted: 28 April 2024  
Published: 1 May 2024



**Copyright:** © 2024 by the authors. Licensee MDPI, Basel, Switzerland. This article is an open access article distributed under the terms and conditions of the Creative Commons Attribution (CC BY) license (<https://creativecommons.org/licenses/by/4.0/>).

## 1. Introduction

Currently, society is developing towards the use of information technology and intelligence, and location services have become an indispensable need. Location-based information services have been used in many applications, such as location-based bicycle sharing, route planning for daily travel, industrial Internet applications, emergency rescue services, road traffic control, and autonomous driving technology. Considering the increasing demand for location-based services, mobile communication technology-based location methods have gradually gained attention [1–3]. In recent years, with the continuous development of 5G technology [4], many studies based on 5G-related technology localization methods have emerged [5–13]. Therefore, 5G-based wireless positioning technology has become a popular topic in current research.

Massive multiple-input multiple-output (MIMO) is an important technology in 5G that increases the resolution in the angular domain through the arrangement of a multitude of antenna arrays at the base station, increasing the aperture of the antenna arrays [14,15], and it achieves better localization results in multipath environments combined with trilateration

or triangulation-based localization methods [16–19]. However, the measurement computation of this method requires the cooperation of multiple base stations, thus generating a large amount of information exchange overhead. To solve this problem, fingerprint-based localization methods [20] have been developed. The fingerprint localization method first constructs a fingerprint database required for localization in the offline phase. Subsequently, the fingerprint user data are matched to the localized signal received in real time with the data in the fingerprint database in the online phase to obtain the coordinates of the user to be localized. Traditional fingerprint data include the received signal strength (RSS) [21]; however, the RSS is susceptible to multipath effects, resulting in low localization accuracy. By contrast, channel state information (CSI)-based fingerprinting [22–25] contains more multipath information than RSS, which can improve the accuracy of localization in multipath environments. In addition, the user can use MIMO technology to obtain high-resolution multipath characteristics in the angular domain of the channel, which improves the strength of the localization signal. In [26], an angle delay channel power matrix (ADCPM) was extracted from the MIMO channel as a fingerprint, and the fingerprint compression method and fingerprint clustering algorithm were combined to realize localization. Consequently, the numerical results verified the reduction in computational complexity and the ability to locate when using the proposed algorithm. In [27], a deep convolutional neural network (DCNN) localization algorithm combining an angular delay channel amplitude matrix (ADCAM) as the fingerprint was proposed, and the results confirmed the high localization accuracy of the algorithm. In [28], a noise reduction strategy was proposed to improve the accuracy of localization using the sparsity of ADCPM fingerprints. The above algorithms can solve the problem of low positioning accuracy caused by multipath signals to a certain extent; however, in the case of a non-line-of-sight (NLOS) path, where direct communication between the base station and the user is absent, the positioning accuracy of the above methods is very poor or even impossible. The intelligent reflective surface (IRS) [29–33], which has received significant attention in recent years, is expected to be the key to solving the problem of the inability to perform localization in an NLOS environment.

The IRS is a programmable meta-surface consisting of a number of low-cost passive reflective elements, which is considered one of the key technologies for 5G and for the realization of wireless smart communication environments towards 6G. Facing the NLOS environment, the signals transmitted by the user to be located can bypass the obstacles by means of the intelligent reflection of the IRS [34]. The phase and amplitude of the signal transmitted by the user to be located can be changed by presetting the reflection coefficient of the smart reflection element through a digital controller. This ensures that the signal propagates along the direction of the base station and is eventually received by the base station [35]. The IRS improves the wireless communication environment by realizing intelligent control of the wireless communication environment in the above way.

Many studies have analyzed enhancements in IRS for the communication environment. In [36], the authors established a wireless channel model based on distributed IRS and proposed a mathematical framework based on the method of moments, analyzed the communication performance of the model such as spectral efficiency and energy efficiency, and demonstrated the advantages and disadvantages of the scheme. In [37], the authors proposed a dual-distributed IRS-assisted communication system that utilizes passive beamforming to optimize the deployment locations of IRSs, thereby maximizing the worst-case Signal-to-Noise Ratio (SNR) at all locations in the target area. In [38], the authors discussed the practical role of IRS for 6G-oriented massive MIMO technology, which is expected to realize all aspects of massive MIMO technology in the upcoming 6G era by exploiting the low-cost maneuverable performance of IRSs. In addition to this, with the continuous development of AI technology, research on AI-assisted IRS communication [39] is ongoing. In [40], a model for IRS communication using deep neural networks was introduced, and the authors verified that a low bit error rate is still obtained with a low signal-to-noise ratio. In [41], the authors used federated learning augmented with deep deterministic policy gradients to optimize IRS deployment and power allocation strategies, and simulations

showed that the algorithm has better convergence rates as well as optimization performance. Therefore, it can be seen that IRSs can enhance the performance of the communication system and improve the communication environment, which plays an important role in the future development of intelligent communication and has great potential to be applied in research on positioning technology [42].

Recently, a number of localization techniques have emerged with regard to the use of IRSs. The authors of [43] investigated the challenges of setting up a fully passive IRS in a wireless network for positioning and showed that with a sufficient number of IRSs, conventional positioning protocols can still function with satisfactory accuracy. In [44], the authors employed a near-field positioning algorithm using large linear IRSs in an NLOS environment to improve signal coverage, and the results show that the method provides good positioning accuracy, even in the presence of high blocking rates. In [45], virtual line-of-sight paths were established using IRSs to maximize the signal reception strength and achieve complete localization in the near field. In [46], the authors used an IRS for RSS-based multiuser positioning and improved the positioning accuracy by amplifying the RSS distribution difference. Although the above literature uses IRSs to improve the wireless signal communication environment and increase the positioning accuracy, it only considers the positioning problem in single-antenna mode and fails to take advantage of MIMO technology.

This study proposes an intelligent reflective surface low-rank matrix reconstruction fingerprint localization (IRS-RFL) algorithm, utilizing the angular-domain power expectation matrix (APEM) as the fingerprint data to leverage the high spatial resolution provided by MIMO technology. In addition, the low-rank matrix fitting (LMaFit) reconstruction algorithm was used to reconstruct the fingerprint database, which solved the problem of the large workload required to build a fingerprint database. Finally, the effectiveness of the proposed positioning scheme was verified through a simulation.

The main contributions of this study are as follows:

- (1) First, this study addresses the problem of a no-direct-line-of-sight path between the base station and the user to be located by constructing an intelligent reflective surface (IRS) 5G positioning system, which consists of a multi-antenna base station and multiple IRSs for signal reflection, and the signal from the user to be located is reflected by the IRSs and reaches the base station. Therefore, this system overcomes the problem that the localization process cannot be performed due to the lack of line-of-sight (LOS) paths.
- (2) Secondly, this study addresses the problem of an excessive workload in fingerprint database construction and uses the LMaFit algorithm for fingerprint database reconstruction. In the fingerprint database construction stage, the fingerprint data consist of APEM, and part of the fingerprint reference points are used to construct the local fingerprint database; then, the complete fingerprint database is reconstructed by its combination with the LMaFit algorithm. This method requires fewer fingerprint data to construct the complete fingerprint database using mathematical operations to reduce the workload of fingerprint database construction.
- (3) In addition, this study increases the gap between fingerprint data by using the maximum ratio combination method, which means that the fingerprint data of each fingerprint reference point are multiplied by their corresponding signal-to-noise ratio (SNR) as the weight, and this facilitates the matching of the data to be compared of the point to be located with the fingerprint data in the fingerprint database in the online matching stage.
- (4) Finally, the simulation results show that the proposed IRS-RFL algorithm achieves sub-meter localization accuracy in a large NLOS complex environment, which is a significant improvement over the traditional fingerprint localization algorithm, thus confirming the good localization effect of the algorithm.

## 2. Materials and Methods

### 2.1. System Model

The 5G positioning system with IRSs is shown in Figure 1 and comprises a base station, IRSs, and the user to be located. It was assumed that there was only one base station in the system, denoted by  $BS$ , with a uniform horizontal linear arrangement of  $W$  antennas, denoted by,  $AN = \{AN_1 \cdots AN_w \cdots AN_W\}$ , where the distance between the antennas is  $d$ . The user to be located in the system was denoted as  $US$  and configured with a single antenna. The system was assumed to be equipped with  $M$  (although, theoretically, an IRS can also continue to localize, in order to improve the accuracy of localization as well as to compare it with TOA/TDOA and other localization methods in subsequent studies, so here we set  $M \geq 3$ ) IRSs, denoted as  $IRS = \{IRS_1 \cdots IRS_m \cdots IRS_M\}$ , where  $IRS_m$  denotes the  $m$ -th IRS, each of which comprised  $K$  reflective units arranged in a uniform horizontal linear pattern, denoted as  $\{IRS_{m,1} \cdots IRS_{m,k} \cdots IRS_{m,K}\}$ . In addition, the distance between the reflective elements is  $d$ . In Figure 1, we use “.....” to denote multiple IRSs to simplify the representation in the figure, and the brown and the blue dotted line with arrows denote the direction of signal transmission from  $US$  to  $IRS$  and  $IRS$  to  $BS$ , respectively.

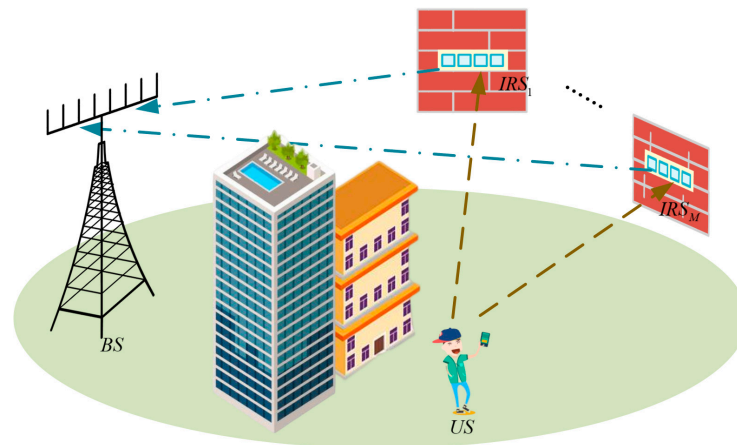


**Figure 1.** 5G positioning system with intelligent reflective surfaces.

Assuming that there was no direct signal path between the user and base station, the user could communicate with the base station through an IRS. The signals received by the base station in this system from the user were divided into two stages: initially from the user to the IRS and subsequently from the IRS to the base station. The two-stage channel was considered a Rayleigh fading channel, and the channel fading coefficient  $\alpha$  was a complex Gaussian random variable with zero mean and  $\sigma_\alpha^2$  variance, that is,  $\alpha \sim \mathcal{CN}(0, \sigma_\alpha^2)$ .

#### 2.1.1. Stage of $US - IRS_m$

The stage from  $US$  transmitting the signal to  $IRS_m$  is referred to as  $US - IRS_m$ , and a signal propagation schematic of this phase is shown in Figure 2.

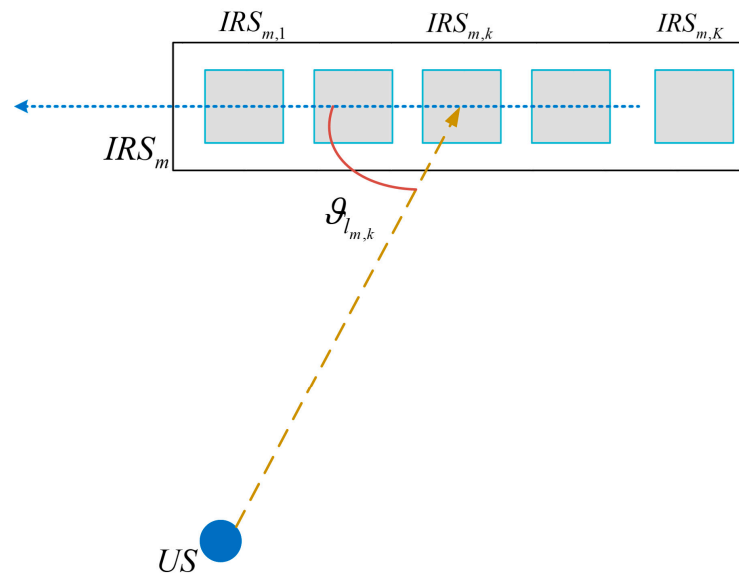


**Figure 2.** Signal propagation schematic of the  $US - IRS_m$  stage.

As shown in Figure 2, the channel from  $US$  to the  $k$ th reflection element of the  $m$ th IRS ( $IRS_m$ ) is denoted as  $h1_{m,k}$ . Its unit is dB, and the specific expression is shown in Equation (1).

$$h1_{m,k} = \sum_{l_{m,k}=1}^{L_{m,k}} \sqrt{\beta1_m} \cdot \alpha1_{l_{m,k}} \cdot e^{-j(k-1)2\pi \frac{d}{\lambda} \cos(\vartheta_{l_{m,k}})}, \tag{1}$$

where  $L_{m,k}$  is the total number of propagation paths (subsequently, the term “propagation paths” will be shortened to “paths”) from  $US$  to the  $k$ th reflecting element of  $IRS_m$ ,  $\beta1_m$  is the large-scale decay factor from  $US$  to  $IRS_m$ ,  $\alpha1_{l_{m,k}}$  is the path fading coefficient of the  $l_{m,k}$ th path,  $\lambda$  is the signal wavelength, and  $\vartheta_{l_{m,k}}$  is the arrival angle of the path  $l_{m,k}$  in a range of  $[0, \pi]$ .

We assume that the total channel in the stage of  $US - IRS_m$  is  $\mathbf{H1}_m \in \mathbb{C}^{K \times 1}$ , where  $\mathbb{C}^{K \times 1}$  denotes the complex matrix of  $K$  rows and 1 column, as shown in Equation (2).

$$\mathbf{H1}_m = [h1_{m,1} \ \cdots \ h1_{m,K}]^T \tag{2}$$

### 2.1.2. Stage of $IRS_m - BS$

It was assumed that the stage from  $IRS_m$  reflected the signal to  $BS$ , which is referred to as the stage of  $IRS_m - BS$ , and a signal propagation schematic of this phase is shown in Figure 3.

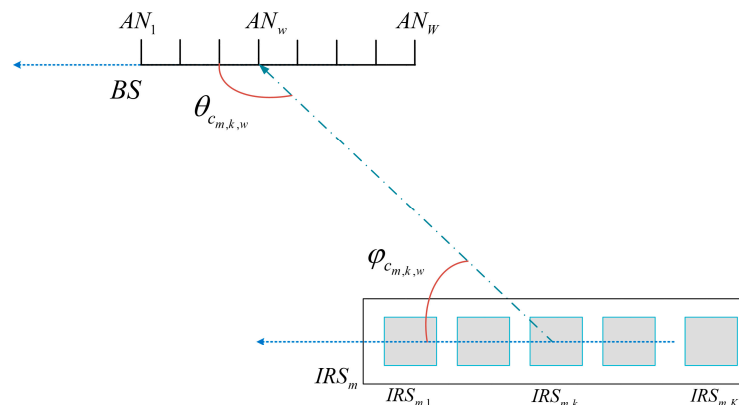


**Figure 3.** Signal propagation schematic of the  $IRS_m - BS$  stage.

As shown in Figure 3, the channel from the  $k$ th reflection element of the  $m$ th IRS ( $IRS_m$ ) to the  $w$ th antenna of  $BS(AN_w)$  is denoted as  $h_{2m,k,w}$ . Its unit is dB, and the specific expression is shown in Equation (3).

$$h_{2m,k,w} = \sum_{c_{m,k,w}=1}^{C_{m,k,w}} \sqrt{\beta_{2m}} \cdot \alpha_{2c_{m,k,w}} \cdot e^{j2\pi \frac{d}{\lambda} [(k-1) \cos(\varphi_{c_{m,k,w}}) + (w-1) \cos(\theta_{c_{m,k,w}})]} \quad (3)$$

where  $C_{m,k,w}$  is the total number of paths from the  $k$ th reflecting element of  $IRS_m$  to the  $w$ th antenna,  $\beta_{2m}$  is the large-scale decay factor from  $IRS_m$  to  $BS$ ,  $\alpha_{2c_{m,k,w}}$  is the path fading coefficient of the  $c_{m,k,w}$ th path,  $\lambda$  is the signal wavelength,  $\theta_{c_{m,k,w}}$  is the arrival angle of the path  $c_{m,k,w}$ , and  $\varphi_{c_{m,k,w}}$  is the launching angle of the path  $c_{m,k,w}$ ; they are all in a range of  $[0, \pi]$ .

We assume that the total channel in the stage of  $IRS_m - BS$  is  $\mathbf{H}_{2m} \in \mathbb{C}^{W \times K}$ , where  $\mathbb{C}^{W \times K}$  denotes the complex matrix of  $W$  rows and  $K$  columns, as expressed in Equation (4). The detailed expression of Equation (4) is shown in (A1) of Appendix A.

$$\mathbf{H}_{2m} = \begin{bmatrix} h_{2m,1,1} & \cdots & h_{2m,K,1} \\ \vdots & \ddots & \vdots \\ h_{2m,1,W} & \cdots & h_{2m,K,W} \end{bmatrix} \quad (4)$$

Therefore, the channel through which the signal emitted by  $US$  arrived at the  $w$ th antenna of  $BS$  via the  $k$ th reflector element of  $IRS_m$  is denoted as  $h_{m,k,w}$ . Its unit is dB, and the specific expression is shown in Equation (5).

$$\begin{aligned} h_{m,k,w} &= h_{1m,k} \cdot \Xi_{m,k} \cdot h_{2m,k,w} \\ &= \sqrt{\beta_m} \sum_{l_{m,k}=1}^{L_{m,k}} \alpha_{1l_{m,k}} \sum_{c_{m,k,w}=1}^{C_{m,k,w}} \alpha_{2c_{m,k,w}} \eta_{m,k} e^{j\omega_{m,k} + j2\pi \frac{d}{\lambda} \{ (k-1)[\cos(\varphi_{c_{m,k,w}}) - \cos(\vartheta_{l_{m,k}})] + (w-1) \cos(\theta_{c_{m,k,w}}) \}} \end{aligned} \quad (5)$$

where  $\beta_m$  is the large-scale fading coefficient from  $US$  through  $IRS_m$  to  $BS$ , and  $\Xi_{m,k}$  is the reflection coefficient of the  $k$ th reflection element of  $IRS_m$ , as expressed in Equation (6).

$$\Xi_{m,k} = \eta_{m,k} e^{j\omega_{m,k}}, \quad (6)$$

where  $\eta_{m,k}$  denotes the reflection amplitude of the  $k$ th reflection element of  $IRS_m$ . In this study, it was assumed that  $\eta_{m,k} = 1$ , so  $\omega_{m,k} \in [0, 2\pi]$  denotes the reflection phase of the  $k$ th reflection element of  $IRS_m$ .

Thus, the total channel of  $IRS_m$ -assisted  $US$  communicating with  $BS$  can be expressed as  $\mathbf{H}_m \in \mathbb{C}^{W \times 1}$ , where  $\mathbb{C}^{W \times 1}$  denotes the complex matrix of  $W$  rows and one column. This is expressed as Equation (7). The detailed expression of Equation (7) is shown in (A2) of Appendix A.

$$\mathbf{H}_m = \mathbf{H}_{2m} \text{diag}(\Xi_m) \mathbf{H}_{1m} = \begin{bmatrix} \sum_{k=1}^K h_{m,k,1} & \cdots & \sum_{k=1}^K h_{m,k,W} \end{bmatrix}^T \quad (7)$$

where  $\text{diag}(\Xi_m)$  represents the reflection coefficient matrix of  $IRS_m$ , expressed as Equation (8).

$$\text{diag}(\Xi_m) = \begin{bmatrix} \eta_{m,1} e^{j\omega_{m,1}} & 0 & 0 \\ 0 & \ddots & 0 \\ 0 & 0 & \eta_{m,K} e^{j\omega_{m,K}} \end{bmatrix}. \quad (8)$$

In addition,

$$\text{diag}(\Xi_m) \mathbf{H}_{1m} = \text{diag}(\mathbf{H}_{1m}) \Xi_m, \quad (9)$$

such that  $\mathbf{Y}_m = \mathbf{H2}_m \text{diag}(\mathbf{H1}_m)$ . Let  $\mathbf{Y}_m \in \mathbb{C}^{W \times K}$  be the cascade channel of  $US - IRS_m - BS$ . Consequently, Equation (7) can be rewritten as Equation (10).

$$\mathbf{H}_m = \mathbf{H2}_m \text{diag}(\mathbf{\Xi}_m) \mathbf{H1}_m = \mathbf{H2}_m \text{diag}(\mathbf{H1}_m) \mathbf{\Xi}_m = \mathbf{Y}_m \mathbf{\Xi}_m \tag{10}$$

where  $\text{diag}(\mathbf{H1}_m)$  is expressed as Equation (11)

$$\text{diag}(\mathbf{H1}_m) = \begin{bmatrix} h_{1,m,1} & 0 & 0 \\ 0 & \ddots & 0 \\ 0 & 0 & h_{1,m,K} \end{bmatrix}. \tag{11}$$

The cascade channel  $\mathbf{Y}_m$  can be transformed from the spatial domain to the angular domain using the Discrete Fourier Transform (DFT) estimation method. Let the DFT matrix at point  $W$  be  $\mathbf{V} \in \mathbb{C}^{W \times W}$ , and let its elements satisfy  $V_{a,b} = e^{-j2\pi \frac{(a-1)(b-1)}{W}}$ . Then, the cascade channel  $\mathbf{Y}_m$  is represented in the angular domain as expressed in Equation (12)

$$\mathbf{Y}_m^{ag} = \mathbf{V} \mathbf{Y}_m, \tag{12}$$

where  $\mathbf{V}$  is expressed as Equation (13)

$$\mathbf{V} = \begin{bmatrix} 1 & \dots & 1 \\ \vdots & \ddots & \vdots \\ 1 & \dots & e^{-j2\pi \frac{(W-1)(W-1)}{W}} \end{bmatrix} \tag{13}$$

where  $\mathbf{Y}_m^{ag} \in \mathbb{C}^{W \times K}$  is the representation of the cascade channel  $\mathbf{Y}_m$  in the angular domain.

Thus, following the reflection through  $IRS_m$ ,  $BS$  received the signal sent by  $US$  as  $\mathbf{Y}_m \in \mathbb{C}^{W \times 1}$ , which is expressed by Equation (14). The detailed expression of Equation (14) is shown in (A3) of Appendix A.

$$\begin{aligned} \mathbf{Y}_m &= \sqrt{\rho} \mathbf{Y}_m^{ag} \mathbf{\Xi}_m s + n' \\ &= \sqrt{\rho} \mathbf{V} \mathbf{Y}_m \mathbf{\Xi}_m s + n' \\ &= \sqrt{\rho} \mathbf{V} \mathbf{H2}_m \text{diag}(\mathbf{H1}_m) \mathbf{\Xi}_m s + n', \end{aligned} \tag{14}$$

where  $\rho$  is the transmit power,  $\mathbf{Y}_m^{ag} \mathbf{\Xi}_m$  is the total channel of  $US - IRS_m - BS$ ,  $s$  is the signal transmitted by  $US$ , and  $n'$  is Gaussian white noise with zero mean and  $\sigma^2$  variance.

## 2.2. IRS-RFL Algorithm

### 2.2.1. Fingerprint Database Construction

Suppose  $N$  fingerprint reference points were uniformly distributed in the IRS-RFL system. Let the coordinate value of the  $n$ th fingerprint reference point be  $\mathbf{LOC}_n = (x_n, y_n, z_n)$ . Then, the signal emitted from this point after reflection by  $IRS_m$  is received by  $BS$  and expressed as  $\mathbf{Y}_{mUS} \in \mathbb{C}^{W \times 1}$ . The corresponding fingerprint data  $\mathbf{f}'_n$  can be represented by Equation (15)

$$\mathbf{f}'_n = [\mathbf{fp}_{1n'}, \dots, \mathbf{fp}_{mn'}, \dots, \mathbf{fp}_{Mn'}], \tag{15}$$

where  $\mathbf{fp}_{mn} = [E(|\mathbf{Y}_{mn}|)]^T$ ,  $|\cdot|$  denotes the modulo operation for each item in the matrix,  $E(\cdot)$  denotes the expectation of the matrix, and  $[\cdot]^T$  denotes the transpose of the matrix. Therefore,  $\mathbf{f}'_n$  is a one-dimensional row vector in the column  $M \times W$ , which, when combined with the coordinate value of the point forms the complete fingerprint  $\mathbf{f}_n$  of the point, is expressed as (16)

$$\mathbf{f}_n = [\mathbf{LOC}_n \ \mathbf{f}'_n]. \tag{16}$$

Let  $LOC = [LOC_1, \dots, LOC_n, \dots, LOC_N]^T$  denote a summary of the coordinate values of the  $N$  fingerprint reference points, which are expressed in Equation (17)

$$LOC = \begin{bmatrix} LOC_1 \\ \vdots \\ LOC_n \\ \vdots \\ LOC_N \end{bmatrix} = \begin{bmatrix} (x_1, y_1, z_1) \\ \vdots \\ (x_n, y_n, z_n) \\ \vdots \\ (x_N, y_N, z_N) \end{bmatrix}_{N \times 3} \tag{17}$$

$F' = [f'_1, \dots, f'_n, \dots, f'_N]^T$  denotes a summary of the fingerprint data from the  $N$  fingerprint reference points, which is expressed by Equation (18)

$$F' = \begin{bmatrix} f'_1 \\ \vdots \\ f'_N \end{bmatrix} = \begin{bmatrix} fp_{11} & \dots & fp_{M1} \\ \vdots & \ddots & \vdots \\ fp_{1N} & \dots & fp_{MN} \end{bmatrix}_{N \times (M \times W)} \tag{18}$$

Consequently, the constructed fingerprint database  $F$  is expressed by Equation (19)

$$F = [LOC \quad F'] = \begin{bmatrix} LOC_1 & f'_1 \\ \vdots & \vdots \\ LOC_N & f'_N \end{bmatrix} \tag{19}$$

### 2.2.2. LMaFit Fingerprint Database Reconstruction Algorithm

When building a fingerprint database, the number of fingerprint reference points is too large, which will lead to a relatively large workload in building the fingerprint database. Therefore, in order to reduce the workload of building a fingerprint database, in this study, we used the LMaFit algorithm to build a complete fingerprint database while only collecting fingerprint data from a partial fingerprint database. The algorithm first samples the fingerprint database  $F'$ , and the number of sampled elements is significantly smaller than the total number of elements  $N \times (M \times W)$  in the fingerprint database  $F'$ . Let  $\Gamma$  be the set of subscripts of the sampled elements. The reconstructed fingerprint database  $X'$ , which is the reconstructed fingerprint database  $F'$ , is obtained following reconstruction using the LMaFit algorithm in the case of the known fingerprint data corresponding to  $\Gamma$ .

Define  $G_\Gamma$  as the projection mapping of the fingerprint database  $F'$  onto  $\Gamma$ .

$$G_\Gamma(F')_{uv} = \begin{cases} F'_{uv}, & (v, u) \in \Gamma \\ 0, & (v, u) \notin \Gamma \end{cases} \tag{20}$$

According to the matrix reconstruction theory, the reconstructed fingerprint database  $X'$  satisfies Equation (21).

$$\begin{aligned} \min \quad & rank(X') \\ s.t. \quad & G_\Gamma(X') = G_\Gamma(F') \end{aligned} \tag{21}$$

where  $\min$  denotes the minimization,  $s.t.$  denotes the constraint, and  $rank(X')$  denotes the rank of  $X'$ . Equation (21) indicates that if there is a unique low-rank matrix  $X'$  satisfying the above conditions, this matrix is the complete estimation matrix of matrix  $F'$ . Considering that this problem is computationally extremely intensive, the LMaFit algorithm was used to transform the rank minimization problem in Equation (21) into the following problem:

$$\begin{aligned} \min \quad & 1/2 \|UR^T - I\|_{F-norm}^2 \\ s.t. \quad & G_\Gamma(I) = G_\Gamma(F') \end{aligned} \tag{22}$$

Let the rank of matrix  $F'$  be  $r$ . We introduce the intermediate matrix  $\mathbf{I}$  to facilitate the calculation and introduce two matrices of dimensions  $N \times r$  and  $(M \times W) \times r$  of  $\mathbf{U}$  and  $\mathbf{R}$  as the matrix to be estimated, that is,  $\mathbf{X}' = \mathbf{UR}^T$ .

Equation (22) is nonconvex and can be transformed into the following Lagrange form for computational convenience:

$$\begin{aligned} L(\mathbf{U}, \mathbf{R}, \mathbf{I}, \mathbf{\Omega}) &= 1/2 \|\mathbf{UR}^T - \mathbf{I}\|_{F\text{-norm}}^2 - \langle \mathbf{\Omega}, G_{\Gamma}(\mathbf{I} - \mathbf{F}') \rangle \\ &= 1/2 \|\mathbf{UR}^T - \mathbf{I}\|_{F\text{-norm}}^2 - \text{trace}(\mathbf{\Omega}^T G_{\Gamma}(\mathbf{I} - \mathbf{F}')), \end{aligned} \tag{23}$$

where  $\langle \mathbf{\Omega}, G_{\Gamma} \rangle = \sum_{a,b} \mathbf{\Omega}_{a,b} (G_{\Gamma})_{a,b}$  is the inner product of matrices, and the matrix  $\mathbf{\Omega}$  is a Lagrange multiplier that satisfies  $\mathbf{\Omega} = G_{\Gamma}(\mathbf{\Omega})$ . As  $\|\mathbf{P}\|_{F\text{-norm}}^2 = \text{trace}(\mathbf{P}^T \mathbf{P})$ , Equation (23) can be transformed into Equation (24) as follows:

$$\begin{aligned} L(\mathbf{U}, \mathbf{R}, \mathbf{I}, \mathbf{\Omega}) &= \frac{1}{2} \text{trace}((\mathbf{U}^T \mathbf{R} - \mathbf{I}^T)(\mathbf{UR}^T - \mathbf{I})) \\ &\quad - \text{trace}(\mathbf{\Omega}^T G_{\Gamma}(\mathbf{I} - \mathbf{F}')) \end{aligned} \tag{24}$$

The above equation is differentiated, and the differential equation is set to 0, which leads to the optimization condition of Equation (22). This can be expressed as Equation (25).

$$\begin{cases} \frac{\partial L}{\partial \mathbf{U}} = (\mathbf{UR}^T - \mathbf{I})\mathbf{R} = 0 \\ \frac{\partial L}{\partial \mathbf{R}} = \mathbf{U}^T(\mathbf{UR}^T - \mathbf{I}) = 0 \\ \frac{\partial L}{\partial \mathbf{\Omega}} = -G_{\Gamma}(\mathbf{I} - \mathbf{F}') = 0 \\ \frac{\partial L}{\partial \mathbf{I}} = \mathbf{U}^T(\mathbf{I} - \mathbf{UR}^T) - \mathbf{\Omega} = 0 \end{cases} \tag{25}$$

Because  $\mathbf{\Omega}_{uv} = 0, (u, v) \notin \Gamma$  exists, the final version of Equation (25) can be written as  $G_{\Gamma^c}(\mathbf{I} - \mathbf{UR}^T) = 0$ , where  $\Gamma^c$  complements  $\Gamma$ .

To solve Equation (25) using the immovable-point iteration method, the first equation in Equation (25) is transformed as follows:

$$\mathbf{UR}^T \mathbf{R} = \mathbf{IR} \tag{26}$$

This equation can be solved as follows:

$$\mathbf{U} = \mathbf{IR}(\mathbf{R}^T \mathbf{R})^+ = \mathbf{I}(\mathbf{R}^+)^T \tag{27}$$

where  $\mathbf{R}^+$  is the Moore–Penrose pseudo-inverse of  $\mathbf{R}$ . Matrix  $\mathbf{U}$  can be updated iteratively according to (27), and similarly, the matrices  $\mathbf{I}$  and  $\mathbf{R}$  can be updated in the iteration using the remaining conditions of Equation (25).

In the convergence calculation process, the approach of dynamically selecting the step size for  $\omega$  at each iteration was adopted as follows. Here,  $\mathbf{E}_{i-1}(\omega)$  denotes the error matrix for the last step size equal to the  $\omega$  iteration, and  $\mathbf{E}_i(\omega)$  is the error matrix for the current step size equal to  $\omega$ . Consequently, the error rate was calculated using Equation (28).

$$\sigma(\omega) = \|\mathbf{E}_i(\omega)\|_{F\text{-norm}} / \|\mathbf{E}_{i-1}(\omega)\|_{F\text{-norm}} \tag{28}$$

In the iterative process, if  $\sigma(\omega) > 1$ , the error is not reduced, and the parameter  $\omega$  is set to 1 in the next iteration. However, if  $\sigma(\omega) \leq 1$ , the error is reduced in the iterative process, and the value of the parameter  $\omega$  in the last iteration was constant. In addition, to obtain a faster iteration speed, the parameter  $\sigma_1$  could be added in the next iteration, and

the value of  $\omega$  could be increased moderately when  $\sigma(\omega) > \sigma_1$ . The stopping criterion of the algorithm is expressed as Equation (29).

$$\frac{\|G_{\Gamma}(\mathbf{X}'_{step} - \mathbf{F}')\|_{F-norm}}{\|G_{\Gamma}(\mathbf{F}')\|_{F-norm}} \leq error, \tag{29}$$

where  $step$  denotes the number of iterations and  $error$  denotes the minimum allowable error.

Thus, the steps of the LMaFit fingerprint database reconstruction algorithm are as Algorithm 1.

---

**Algorithm 1** LMaFit Fingerprint Database Reconstruction Algorithm

---

Input: Fingerprint database  $\mathbf{F}'$  set of subscripts of the sampled elements  $\Gamma$  sampled fingerprint database  $G_{\Gamma}(\mathbf{F}')$ , iteration step  $\omega$ , maximum number of iterations  $step(\zeta = 1, \dots, step)$ , allowed minimum error  $error$ , initialization:  $\mathbf{U}, \mathbf{R}, \mathbf{I}$

Repeat:

1. Update the error matrix  $\mathbf{E}$  using equation  $\mathbf{E}_{\zeta+1} = G_{\Gamma}(\mathbf{F}' - \mathbf{U}_{\zeta}\mathbf{R}_{\zeta}^T)$ .
2. Update the intermediate matrix  $\mathbf{I}$  using equation  $\mathbf{I}_{\zeta+1} = \mathbf{U}_{\zeta}\mathbf{R}_{\zeta} + \omega\mathbf{E}_{\zeta+1}$ .
3. Update the matrix  $\mathbf{U}$  using equation  $\mathbf{U}_{\zeta+1} = \omega\mathbf{I}_{\zeta+1}\mathbf{R}_{\zeta}(\mathbf{R}_{\zeta}^T\mathbf{R}_{\zeta})^{-1} + (1 - \omega)\mathbf{U}_{\zeta}$ .
4. Update the matrix  $\mathbf{R}$  using equation  $\mathbf{R}_{\zeta+1} = \omega\mathbf{I}_{\zeta+1}^T\mathbf{U}_{\zeta+1}(\mathbf{U}_{\zeta+1}^T\mathbf{U}_{\zeta+1})^{-1} + (1 - \omega)\mathbf{R}_{\zeta}$ .

Until: The maximum number of iterations  $step$  is reached or is less than the minimum allowable error  $error$ .

Output: Reconstructed fingerprint database  $\mathbf{X}' = \mathbf{U}\mathbf{R}^T$ .

---

After obtaining the reconstructed fingerprint database  $\mathbf{X}'$ , the complete reconstructed fingerprint database  $\mathbf{X}$  was obtained by merging it with its corresponding coordinates, as shown in Equation (30).

$$\mathbf{X} = [\mathbf{LOC} \quad \mathbf{X}']. \tag{30}$$

### 2.2.3. Online Matching Positioning Stage

Let the coordinates of  $US$  be  $\mathbf{LOC}_{US} = (x_{US}, y_{US}, z_{US})$ , and the data to be compared are  $\mathbf{f}'_{US} = [\mathbf{fp}_{1US}, \dots, \mathbf{fp}_{MUS}]$ . The data combined with the coordinates of  $US$  and the data to be compared of  $US$  are expressed as Equation (31).

$$\mathbf{f}_{US} = [\mathbf{LOC}_{US}, \mathbf{fp}_{1US}, \dots, \mathbf{fp}_{MUS}]. \tag{31}$$

The reconstructed fingerprint database  $\mathbf{X}'$  was obtained in the offline database building stage, and the online matching and positioning stage employed the maximum ratio [47] merging concept to multiply the fingerprint data of each fingerprint reference point with the corresponding SNR. Here, the SNR  $SNR_m$  denotes the SNR of the channel between  $US$  and  $BS$  after reflection through  $IRS_m$ . Its calculation is given by Equation (32).

$$SNR_m = \frac{\|\mathbf{H}_m\|^2}{\sigma^2}, \tag{32}$$

where  $\sigma^2$  denotes the average power of the noise.

The data to be compared from the  $US$ , combined with the maximum ratio, were then matched to assess similarity with the fingerprint data in the fingerprint database using the WKNN algorithm. Euclidean distance was used to measure the similarity of fingerprints. A larger distance implied lower similarity, whereas a smaller distance implied a higher similarity. Let  $\mathbf{X}_i = [\mathbf{fp}_{1i}, \dots, \mathbf{fp}_{Mi}]$  be the  $i$ th fingerprint data in the reconstructed

fingerprint database  $\mathbf{X}$ . The formula for calculating the similarity between the data to be compared of  $US$  and the  $i$ th fingerprint data is:

$$sim_i = \sqrt{\sum_{m=1}^M \sum_{w=1}^W (fp_{mi}(m, w)SNR_{mi} - fp_{mUS}(m, w)SNR_m)^2} \quad (33)$$

where  $SNR_{im}$  is the SNR of  $BS$  to the channel of the  $i$ th fingerprint reference point after reflection through  $IRS_m$ . Following the similarity measurements with all fingerprint data points in the database, the coordinates  $[LOC_1, \dots, LOC_S]$  corresponding to the  $S$  ( $S \geq 3$ ) fingerprint data points with the highest similarity were selected. Subsequently, the WKNN algorithm was used to assign different weights (*weight*) to the coordinates corresponding to fingerprint data points with different similarities, which were calculated using Equation (34).

$$weight_s = \frac{1/(sim_s + \epsilon)}{\sum_{s=1}^S 1/(sim_s + \epsilon)}, \quad (34)$$

where  $\epsilon$  is a small positive number used to avoid a zero denominator. After obtaining the corresponding weights of the coordinates of the  $S$  reference points, the estimated coordinates  $LOC'_{US}$  of  $US$  can be obtained using Equation (35).

$$\begin{aligned} LOC'_{US} &= (x'_{US}, y'_{US}, z'_{US}) \\ &= \sum_{s=1}^S weight_s LOC_s \end{aligned} \quad (35)$$

The localization error  $e'$  was calculated using the Euclidean distance between the estimated coordinates of  $US$  and true coordinates of  $US$ , as expressed by Equation (36).

$$e' = \sqrt{(x_{US} - x'_{US})^2 + (y_{US} - y'_{US})^2 + (z_{US} - z'_{US})^2} \quad (36)$$

### 3. Experimental Results and Analysis

The MATLAB R2021b simulation platform was used to simulate and verify the proposed IRS-RFL algorithm. The simulation environment is set to  $100 \text{ m} \times 100 \text{ m} \times 15 \text{ m}$  three-dimensional space as shown in Figure 4. In this study, the flat fading Rayleigh channel is used in the simulation verification. The fingerprint data in the set positioning space were sampled on a grid with a sampling interval of  $\gamma = 1 \text{ m}$ . The parameters were set as follows: number of antennas  $BS$  of  $K = 8$ , spacing  $d = \frac{\lambda}{2}$ , number of paths  $C = 3$  of  $BS - IRS$ , average power of noise  $-96 \text{ dBm}$ , carrier frequency  $f_c = 3.5 \text{ GHz}$ ; the total number of  $IRS$ s is  $M = 9$ , where the coordinates of  $IRS_1 - IRS_9$  are  $(0 \text{ m}, 75 \text{ m}, 15 \text{ m})$ ,  $(100 \text{ m}, 0 \text{ m}, 15 \text{ m})$ ,  $(100 \text{ m}, 100 \text{ m}, 15 \text{ m})$ ,  $(100 \text{ m}, 50 \text{ m}, 15 \text{ m})$ ,  $(75 \text{ m}, 100 \text{ m}, 15 \text{ m})$ ,  $(0 \text{ m}, 50 \text{ m}, 15 \text{ m})$ ,  $(50 \text{ m}, 0 \text{ m}, 15 \text{ m})$ ,  $(25 \text{ m}, 100 \text{ m}, 15 \text{ m})$ ,  $(100 \text{ m}, 75 \text{ m}, 15 \text{ m})$ . And the number of reflective elements  $W = 8$  of each  $IRS$ , and number of paths  $L = 3$  of  $IRS - US$ . The large-scale decay coefficient was  $\beta_{mUS} = -86.65 - 20 \log_{10}(dis_{IRS_m, US} \cdot dis_{BS, IRS_m}) + \chi_{mUS} [\text{dB}]$  [48], where  $dis_{IRS_m, US}$  is the distance between  $US$  and  $IRS_m$ ,  $dis_{BS, IRS_m}$  is the distance between  $BS$  and  $IRS_m$ , and  $\chi_{mUS} \sim \mathcal{CN}(0, 64)$  is the shadow decay.

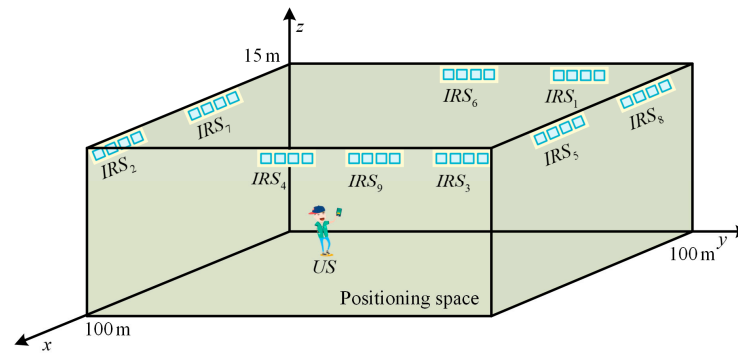


Figure 4. IRS simulation modelling general layout.

3.1. Simulation of Algorithm for Reconstructing Fingerprint Database

When constructing the fingerprint database, first, the original fingerprint database  $F'$  was obtained. Then, 60% of the data were randomly sampled to recover the remaining data and obtain the reconstructed fingerprint database  $X'$ . Because of the large size of the fingerprint database, it only provides data from some fingerprint reference points for comparison. The fingerprint data from the original fingerprint database are listed in Table 1. The data in the reconstructed fingerprint database are listed in Table 2. The absolute errors of some data between the reconstructed and original fingerprint databases are listed in Table 3.

Table 1. Original fingerprint matrix data.

	1	2	3	4	5	6	7	8
1	166.1103	142.2683	162.862	148.1069	1585.3218	161.5227	176.1805	169.7322
2	165.7726	190.1619	199.2585	181.5946	1765.6832	176.7504	206.7448	179.3109
3	162.6964	153.8574	167.5265	164.2221	1679.1405	154.9969	163.9783	160.0116
4	187.4405	168.8461	171.5338	207.7941	1860.735	215.5813	198.855	196.7667
5	190.54	162.0931	205.4878	174.8375	1864.1001	222.0865	202.3262	182.3111
6	190.0572	167.0714	146.0369	162.1234	1690.4696	147.1783	163.1289	159.0874

Table 2. Reconstructed fingerprint matrix data.

	1	2	3	4	5	6	7	8
1	166.1103	142.2683	162.862	148.1069	1585.3218	161.5227	179.0332	169.7322
2	165.7726	188.7121	199.2585	181.5946	1765.6832	176.7504	206.7448	179.3109
3	165.4293	153.8574	165.2193	164.7294	1679.1405	154.9969	164.7676	164.692
4	187.4405	168.8461	171.5338	207.7941	1860.735	215.5813	193.9373	193.8484
5	190.54	162.0931	205.4878	174.8375	1864.1001	222.0865	202.3262	183.9541
6	190.0572	161.6099	146.0369	161.6529	1690.4696	147.1783	161.6904	161.6163

Table 3. Absolute error data.

	1	2	3	4	5	6	7	8
1	0	0	0	0	0	0	-2.8527	0
2	0	1.4498	0	0	0	0	0	0
3	-2.7329	0	2.3072	-0.5073	0	0	-0.7893	-4.6804
4	0	0	0	0	0	0	4.9177	2.9183
5	0	0	0	0	0	0	0	-1.643
6	0	5.4615	0	0.4705	0	0	1.4385	-2.5289

As shown in Tables 3 and 4, an error existed between the reconstructed and original fingerprint databases, and the average relative error calculated from all the data was 1.85%; therefore, there was almost no effect on the localization error.

**Table 4.** Relative error data.

	1	2	3	4	5	6	7	8
1	0	0	0	0	0	0	1.62%	0
2	0	0.76%	0	0	0	0	0	0
3	1.68%	0	1.38%	0.31%	0	0	0.48%	2.93%
4	0	0	0	0	0	0	2.47%	1.48%
5	0	0	0	0	0	0	0	0.9%
6	0	3.27%	0%	0.29%	0	0	0.88%	1.59%

### 3.2. Analysis of Algorithm for Reconstructing Fingerprint Database

1. The localization of fingerprint databases without a reconstruction algorithm (IRS-URFL) and the complexity of constructing database fingerprints are as follows:

In the fingerprint database construction phase, when the matrix reconstruction algorithm is not used to construct the fingerprint database  $F'$ , the total number of elements in the fingerprint database  $F'$  is  $NMW$ , and the generation of each fingerprint data requires approximately  $W \cdot K \cdot L \cdot \text{times}$  floating-point computations, where *times* is the number of times each fingerprint datum is sampled. Therefore, the number of floating-point calculations for the process is approximated as  $O(W^2 \cdot K \cdot N \cdot M \cdot L \cdot \text{times})$ .

2. Reconstructing the fingerprint database using the LMaFit algorithm for the indoor radio signal-based robust fingerprint localization (IRS-RFL) algorithm, the complexity of constructing database fingerprints is as follows:

When using the matrix reconstruction algorithm for constructing the fingerprint database, we first collect 60% of the fingerprint database  $F'$ , and the computational complexity required for this process is about  $O(0.6W^2 \cdot K \cdot N \cdot M \cdot L \cdot \text{times})$ . Then, we use the LMaFit algorithm to complement the remaining 40% of the fingerprint data, and in this way, we reconstruct to obtain the complete fingerprint database  $X'$ .

The floating-point operations of the LMaFit algorithm are divided into two main parts: matrix factorization and matrix data reconstruction through multiple iterations. In this study, firstly, the number of floating-point operations in the matrix factorization part is  $O(N(MW)^2)$ . Secondly, the part of the matrix data reconstruction through multiple iterations mainly involves calculating the update parameters and performing matrix multiplication operations, so the number of floating-point operations in this part is  $O(\text{step}(N(MW)^2))$ , where *step* is the number of iterations. Thus, the number of floating-point computations using the LMaFit matrix reconstruction algorithm can be approximated as  $O(N(MW)^2 + \text{step}(N(MW)^2))$ .

Therefore, the total number of floating-point operations when using the matrix reconstruction algorithm for constructing the fingerprint database  $X'$  is approximated by  $O(0.6W^2 \cdot K \cdot N \cdot M \cdot L \cdot \text{times} + N(MW)^2 + \text{step}(N(MW)^2))$ .

3. Complexity comparison:

Therefore, theoretically,  $M = 5$ ,  $W = 8$ ,  $K = 8$ ,  $L = 3$ ,  $\text{times} = 21$ ,  $\text{step} = 35$ . At this time, the computational complexity of the IRS-URFL algorithm and IRS-RFL algorithm is shown below.

In Figure 5, the horizontal coordinates represent the number of rows in the matrix, and the vertical coordinates represent the computational complexity of the algorithms; the blue line represents the computational complexity of constructing the fingerprint database when the localization (IRS-URFL) algorithm for fingerprint databases is used without

the reconstruction algorithm; and the red line represents the computational complexity of constructing the fingerprint database when the localization (IRS-RFL) algorithm for fingerprint databases is reconstructed using the low-rank matrix fitting (LMaFit) algorithm. The computational complexity of the fingerprint database was also considered. From the figure, it can be seen that as the number of matrix rows increases, the computational complexity of the IRS-RFL algorithm is small compared to the computational complexity of the IRS-URFL algorithm. For example, when  $N = 15,000$ , the computational complexity of the IRS-RFL algorithm is reduced by about  $2.4 \times 10^8$  computations compared to that of the IRS-URFL algorithm, and, therefore, the IRS-RFL algorithm reduces the amount of work involved in constructing the fingerprint database, where the number of rows in the matrix affects the number of matrix elements. As the number of matrix elements increases, the complexity of the algorithm for constructing the matrix also increases.

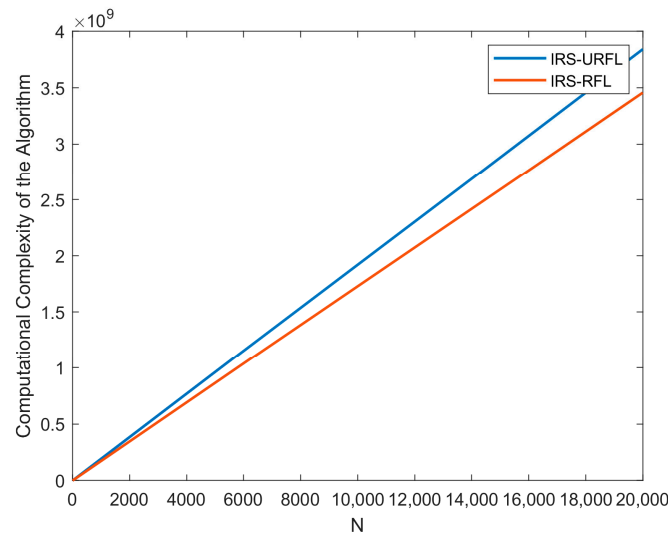


**Figure 5.** Comparison of computational complexity between IRS-URFL algorithm and IRS-RFL algorithm.

### 3.3. Simulation of Positioning Errors

When  $SNR = 10$  dB, the localization results of the IRS-RFL algorithm in this study are shown in Figure 6, where the asterisk indicates the estimated location of the point to be located, and the hollow point indicates the real location of the point to be located.

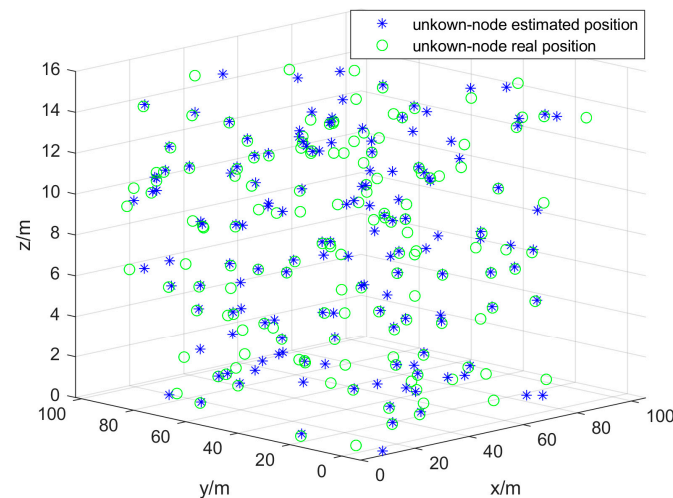


**Figure 6.** Schematic of the localization result of the IRS-RFL algorithm.

As shown in Figure 6, the point to be located that was estimated by the proposed IRS-RFL algorithm was similar to or overlapped with most of the real locations. This indicated the highly accurate localization results of the proposed IRS-RFL algorithm.

Positioning error analysis plots of the traditional fingerprint localization (traditional RSS) algorithm [49–51], the intelligent reflective surface for unreconstructed fingerprint localization (IRS-URFL) algorithm, and IRS-RFL algorithm are shown in Figure 7.

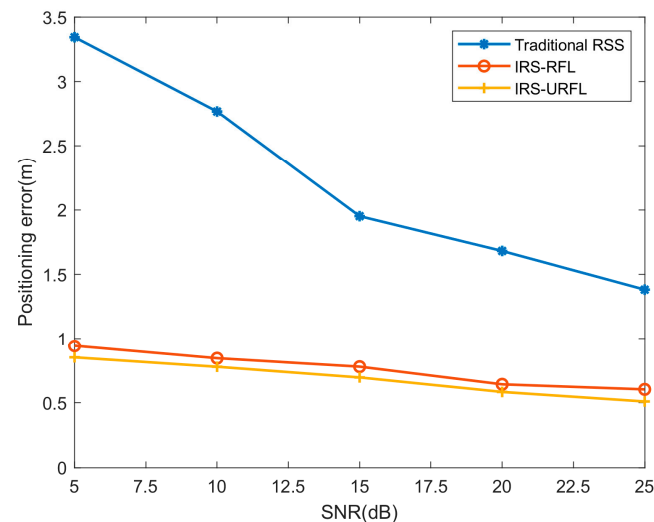


**Figure 7.** Positioning error of different positioning methods.

In Figure 7, the horizontal coordinate, vertical coordinate, blue curve, red curve, and yellow curve indicate the SNR (dB), positioning error (m), positioning error of the traditional RSS algorithm, positioning error of the IRS-RFL algorithm, and positioning error of the IRS-URFL algorithm, respectively. The results show that at  $SNR = 5$  dB, the error of the traditional RSS algorithm is 3.35 m, the error of the IRS-RFL algorithm is 0.97 m, and the error of the IRS-URFL algorithm is 0.92 m; at  $SNR = 25$  dB, the error of the traditional RSS algorithm is 1.41 m, the error of the IRS-RFL algorithm is 0.60 m, the error of the IRS-URFL algorithm is 0.92 m, and the IRS-URFL algorithm has an error of 0.57 m. All three localization algorithms show better localization results as the SNR increases. Among these three algorithms, the IRS-URFL algorithm has the highest positioning accuracy and the smallest positioning error, and the IRS-RFL algorithm has a higher positioning accuracy than the traditional RSS algorithm. First of all, both the IRS-URFL algorithm and IRS-RFL algorithm use APEM fingerprints; this type of fingerprint contains more information compared to RSS fingerprints, and the correspondence between this information and spatial location is stronger, which is conducive to improving the system's localization accuracy, so the localization error of the traditional RSS algorithm is higher than the IRS-URFL algorithm and IRS-RFL algorithm's positioning error. In addition, because the IRS-RFL algorithm uses the LMAfit reconstruction algorithm, there is a certain error between the reconstructed fingerprint database and the fingerprint database that is directly collected without reconstruction; therefore, the IRS-RFL algorithm has a larger localization error than the IRS-URFL algorithm compared to the IRS-RFL algorithm.

The localization errors for different numbers of IRS and SNRs are shown in Figure 8.

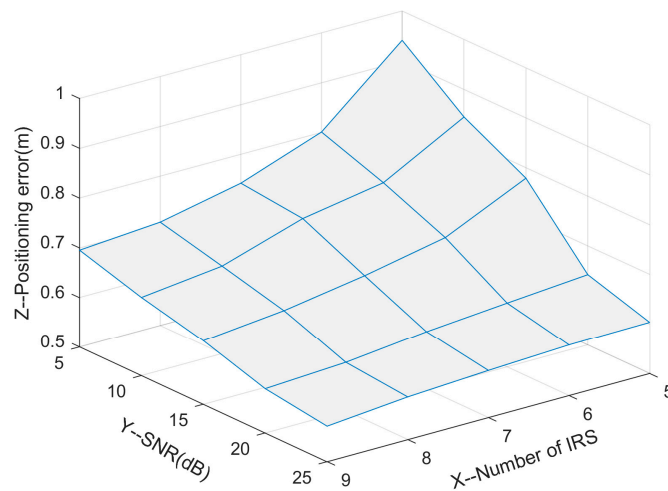


**Figure 8.** Positioning error for different numbers of IRS cases.

As shown in Figure 8, the X, Y, and Z coordinates indicate the number of IRSs, SNRs (dB), and localization errors (m), respectively. The figure shows that with an increase in the SNR number of IRSs, the localization error of the IRS-RFL algorithm gradually decreases. For IRS  $M = 6$ , the localization error was less than 1 m, and it decreased gradually with an increase in SNR; when  $SNR = 15$ , the localization error decreased gradually with an increase in IRS. This shows that both SNR and the number of IRSs have a highly significant effect on the localization accuracy. In the wireless communication system, SNR indicates the power ratio of the received signal to the noise, and the larger the SNR, the stronger the useful signal in the received signal and the smaller the interference generated by the noise. In this case, the fingerprint APEM will be inaccurate, and the final localization error of the IRS-RFL algorithm in this study will be larger. In contrast, the smaller the SNR, the less useful the signal received. The number of IRSs has an impact on the number of fingerprints collected; the higher the number of IRSs, the higher the number of fingerprints, and an increase in the number of fingerprints can improve the localization accuracy.

The cumulative distribution of the localization error of IRS-RFL at different sampling intervals is shown in Figure 9.

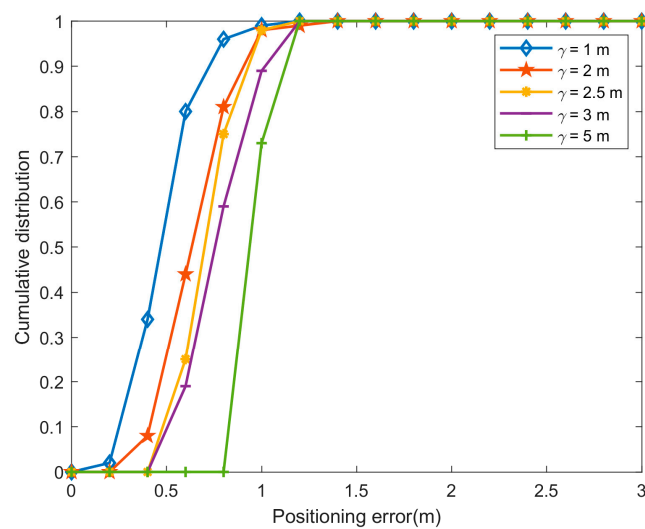


**Figure 9.** Cumulative distribution of positioning errors at different sampling intervals.

Figure 9 shows the cumulative distribution of the positioning error at different sampling intervals. The blue, red, yellow, purple, and green curves indicate the cumulative

distribution function curves of the positioning error for sampling intervals of 1, 2, 2.5, 3, and 5 m, respectively. Evidently, the sampling interval was inversely proportional to the positioning error; the larger the sampling interval, the worse the positioning accuracy. For sampling intervals of 5, 3, 2.5, 2, and 1 m, 80% of the positioning errors were less than 1.2, 1, 0.83, 0.8, and 0.6 m, respectively. In fingerprint localization, the sampling interval of the fingerprints has an impact on the number of fingerprints collected. The smaller the sampling interval, the higher the localization accuracy of the system, and, on the contrary, the worse the positioning accuracy of the system. When the sampling interval is short, the 5G positioning system with intelligent reflective surfaces proposed in this study can increase the number of fingerprints, thereby improving the accuracy and reliability of positioning. On the contrary, when the sampling interval is longer, the number of fingerprints collected by the intelligent reflective surface 5G positioning system proposed in this study decreases, which does not accurately reflect the accurate information of the channel of each point in the positioning area, thus reducing the localization accuracy.

#### 4. Conclusions

In this study, we proposed a low-rank matrix reconstruction-enabled fingerprint-based localization algorithm in IRS-assisted networks, which used APEM as fingerprint data and exploited the high spatial resolution of MIMO technology. The LMaFit matrix reconstruction algorithm was used to reconstruct the fingerprint database to alleviate the large workload introduced by the full set of measurement data required to build a fingerprint database and reduce the workload of fingerprint acquisition. The similarity of fingerprints was determined using the Euclidean distance, and the coordinates of the users to be located were estimated by combining maximal ratio combining and WKNN algorithms. Finally, it was verified through simulation that the proposed method can reduce the fingerprint database construction workload by 40%, and it has an 80% probability of obtaining sub-meter localization accuracy when the sampling interval is less than 2.5 m.

**Author Contributions:** Conceptualization, S.D. and Y.Z.; methodology, S.D. and Y.Z.; validation, S.D.; formal analysis, S.D.; investigation, S.D.; writing—original draft preparation, S.D. and Y.Z. and R.L.; supervision, Y.Z. and R.L.; funding acquisition, Y.Z. All authors have read and agreed to the published version of the manuscript.

**Funding:** This work was supported, in part, by the Sub Project of National Key Research and Development plan in 2020. NO. 2020YFC1511704, Beijing Information Science & Technology University NO. 2020KYNH212, NO. 2021CGZH302, Beijing Science and Technology Project (Grant No. Z211100004421009), and, in part, by the National Natural Science Foundation of China (Grant No. 61971048).

**Data Availability Statement:** Data is contained within the article.

**Conflicts of Interest:** Author Ruiqi Liu was employed by the company ZTE Corporation. The remaining authors declare that the research was conducted in the absence of any commercial or financial relationships that could be construed as a potential conflict of interest.

#### Appendix A. Specific expression of Equations (4), (7) and (14)

The detailed expression of Equations (4), (7) and (14) is shown in (A1), (A2) and (A3), separately.

$$\begin{aligned}
 & \mathbf{H2}_m \\
 &= \begin{bmatrix} h_{2m,1,1} & \cdots & h_{2m,K,1} \\ \vdots & \ddots & \vdots \\ h_{2m,1,W} & \cdots & h_{2m,K,W} \end{bmatrix} \\
 &= \sqrt{\beta_{2m}} \cdot \begin{bmatrix} \sum_{c_{m,1,1}=1}^{C_{m,1,1}} \alpha_{2c_{m,1,1}} & \cdots & \sum_{c_{m,K,1}=1}^{C_{m,K,1}} \alpha_{2c_{m,K,1}} \cdot e^{j2\pi \frac{d}{\lambda} [(K-1) \cos(\varphi_{c_{m,K,1}})]} \\ \vdots & \ddots & \vdots \\ \sum_{c_{m,1,W}=1}^{C_{m,1,W}} \alpha_{2c_{m,1,W}} \cdot e^{j2\pi \frac{d}{\lambda} [(W-1) \cos(\theta_{c_{m,1,W}})]} & \cdots & \sum_{c_{m,K,W}=1}^{C_{m,K,W}} \alpha_{2c_{m,K,W}} \cdot e^{j2\pi \frac{d}{\lambda} [(K-1) \cos(\varphi_{c_{m,K,W}}) + (W-1) \cos(\theta_{c_{m,K,W}})]} \end{bmatrix} \quad (A1)
 \end{aligned}$$

$$\begin{aligned}
 & \mathbf{H}_m \\
 &= \mathbf{H2}_m \mathbf{diag}(\Xi_m) \mathbf{H1}_m \\
 &= \begin{bmatrix} \sum_{k=1}^K h_{m,k,1} & \cdots & \sum_{k=1}^K h_{m,k,W} \end{bmatrix}^T \\
 &= \sqrt{\beta_m} \cdot \begin{bmatrix} \sum_{k=1}^K \sum_{l_{m,k}=1}^{L_{m,k}} \alpha_{1l_{m,k}} \sum_{c_{m,k,1}=1}^{C_{m,k,1}} \alpha_{2c_{m,k,1}} \eta_{m,k} e^{j\omega_{m,k} + j2\pi \frac{d}{\lambda} \{ (k-1)[\cos(\varphi_{c_{m,k,1}}) - \cos(\theta_{l_{m,k}})] \}} \\ \vdots \\ \sum_{k=1}^K \sum_{l_{m,k}=1}^{L_{m,k}} \alpha_{1l_{m,k}} \sum_{c_{m,k,W}=1}^{C_{m,k,W}} \alpha_{2c_{m,k,W}} \eta_{m,k} e^{j\omega_{m,k} + j2\pi \frac{d}{\lambda} \{ (k-1)[\cos(\varphi_{c_{m,k,W}}) - \cos(\theta_{l_{m,k}})] + (W-1) \cos(\theta_{c_{m,k,W}}) \}} \end{bmatrix} \quad (A2)
 \end{aligned}$$

$$\begin{aligned}
 & \mathbf{Y}_m \\
 &= \sqrt{\rho} \mathbf{Y}_m^{sig} \Xi_m \mathbf{s} + \mathbf{n}' \\
 &= \sqrt{\rho} \mathbf{V} \mathbf{Y}_m \Xi_m \mathbf{s} + \mathbf{n}' \\
 &= \sqrt{\rho} \mathbf{V} \mathbf{H2}_m \mathbf{diag}(\mathbf{H1}_m) \Xi_m \mathbf{s} + \mathbf{n}' \\
 &= \sqrt{\rho \beta_m} \cdot \begin{bmatrix} \sum_{k=1}^K \sum_{w=1}^W \sum_{l_{m,k}=1}^{L_{m,k}} \alpha_{1l_{m,k}} \sum_{c_{m,k,w}=1}^{C_{m,k,w}} \alpha_{2c_{m,k,w}} \eta_{m,k} e^{j\omega_{m,k} + j2\pi \frac{d}{\lambda} \{ (k-1)[\cos(\varphi_{c_{m,k,w}}) - \cos(\theta_{l_{m,k}})] + (w-1) \cos(\theta_{c_{m,k,w}}) \}} \\ \vdots \\ \sum_{k=1}^K \sum_{w=1}^W \sum_{l_{m,k}=1}^{L_{m,k}} \alpha_{1l_{m,k}} \sum_{c_{m,k,w}=1}^{C_{m,k,w}} \alpha_{2c_{m,k,w}} \eta_{m,k} e^{j\omega_{m,k} + j2\pi \frac{d}{\lambda} \{ (k-1)[\cos(\varphi_{c_{m,k,w}}) - \cos(\theta_{l_{m,k}})] + (w-1) \cos(\theta_{c_{m,k,w}}) \}} - j2\pi \frac{(w-1)(W-1)}{W} \end{bmatrix} \mathbf{s} + \mathbf{n}' \quad (A3)
 \end{aligned}$$

References

1. Del Peral-Rosado, J.A.; Raulefs, R.; López-Salcedo, J.A.; Seco-Granados, G. Survey of Cellular Mobile Radio Localization Methods: From 1G to 5G. *IEEE Commun. Surv. Tut.* **2018**, *20*, 1124–1148. [\[CrossRef\]](#)
2. Traboulsi, S. Overview of 5G-oriented Positioning Technology in Smart Cities. *Procedia Comput. Sci.* **2022**, *201*, 368–374. [\[CrossRef\]](#)
3. Deng, Z.; Zheng, X.; Wang, H.; Fu, X.; Yin, L.; Liu, W. A Novel Time Delay Estimation Algorithm for 5G Vehicle Positioning in Urban Canyon Environments. *Sensors* **2020**, *20*, 5190. [\[CrossRef\]](#)
4. Liu, Y.; Shi, X.; He, S.; Shi, Z. Prospective Positioning Architecture and Technologies in 5G Networks. *IEEE Netw.* **2017**, *31*, 115–121. [\[CrossRef\]](#)
5. Dwivedi, S.; Shreevastav, R.; Munier, F.; Nygren, J.; Siomina, I.; Lyazidi, Y.; Shrestha, D.; Lindmark, G.; Ernström, P.; Stare, E.; et al. Positioning in 5G Networks. *IEEE Commun. Mag.* **2021**, *59*, 38–44. [\[CrossRef\]](#)
6. Koivisto, M.; Costa, M.; Werner, J.; Heiska, K.; Talvitie, J.; Leppänen, K.; Koivunen, V.; Valkama, M.; Member, S. Joint Device Positioning and Clock Synchronization in 5G Ultra-Dense Networks. *IEEE Trans. Wirel. Commun.* **2017**, *16*, 2866–2881. [\[CrossRef\]](#)
7. Shamaei, K.; Kassas, Z.M. Receiver Design and Time of Arrival Estimation for Opportunistic Localization with 5G Signals. *IEEE Trans. Wirel. Commun.* **2021**, *20*, 4716–4731. [\[CrossRef\]](#)
8. Zhang, Z.Y.; Kang, S.L. Time of arrival estimation based on clustering for positioning in OFDM system. *IET Commun.* **2020**, *14*, 2584–2591. [\[CrossRef\]](#)
9. Gong, Y.; Zhao, H.; Hu, K.; Lu, Q.; Shen, Y. A Multipath-Aided Localization Method for MIMO-OFDM Systems via Tensor Decomposition. *IEEE Wirel. Commun. Lett.* **2022**, *11*, 1225–1228. [\[CrossRef\]](#)
10. Zhao, B.; Hu, K.; Gong, Y.; Shen, Y. A Tensor-Based Joint AoA and ToF Estimation Method for Wi-Fi Systems. *IEEE Wirel. Commun. Lett.* **2021**, *10*, 2543–2546. [\[CrossRef\]](#)

11. Shen, J.; Molisch, A.F.; Salmi, J. Accurate Passive Location Estimation Using TOA Measurements. *IEEE Trans. Wirel. Commun.* **2012**, *11*, 2182–2192. [[CrossRef](#)]
12. Zhang, L.; Zhang, T.; Shin, H.S. An Efficient Constrained Weighted Least Squares Method With Bias Reduction for TDOA-Based Localization. *IEEE Sens. J.* **2021**, *21*, 10122–10131. [[CrossRef](#)]
13. Chen, C.Y.; Wu, W.R. Three-Dimensional Positioning for LTE Systems. *IEEE Trans. Veh. Technol.* **2017**, *66*, 3220–3234. [[CrossRef](#)]
14. Wen, F.; Wymeersch, H.; Peng, B.; Tay, W.P.; Cheung So, H.; Yang, D. A survey on 5G massive MIMO localization. *Digit. Signal Process.* **2019**, *94*, 21–28. [[CrossRef](#)]
15. Liu, R.; Zhang, C.; Song, J. Line of Sight Component Identification and Positioning in Single Frequency Networks Under Multipath Propagation. *IEEE Trans. Broadcast.* **2019**, *65*, 220–233. [[CrossRef](#)]
16. Li, J.; Conan, J.; Pierre, S. Position location of mobile terminal in wireless MIMO communication systems. *J. Commun. Netw.* **2007**, *9*, 254–264. [[CrossRef](#)]
17. Garcia, N.; Wymeersch, H.; Larsson, E.G.; Haimovich, A.M.; Coulon, M. Direct Localization for Massive MIMO. *IEEE Trans. Signal Process.* **2017**, *65*, 2475–2487. [[CrossRef](#)]
18. Liang, J.; He, J.; Yu, W.; Truong, T.K. Single-Site 3-D Positioning in Multipath Environments Using DOA-Delay Measurements. *IEEE Commun. Lett.* **2021**, *25*, 2559–2563. [[CrossRef](#)]
19. Hu, A.; Lv, T.; Gao, H.; Zhang, Z.; Yang, S. An ESPRIT-Based Approach for 2-D Localization of Incoherently Distributed Sources in Massive MIMO Systems. *IEEE J. Sel. Top. Signal Process.* **2014**, *8*, 996–1011. [[CrossRef](#)]
20. Shen, Z.; Xu, K.; Xia, X. 2D Fingerprinting-Based Localization for mmWave Cell-Free Massive MIMO Systems. *IEEE Commun. Lett.* **2021**, *25*, 3556–3560. [[CrossRef](#)]
21. Zhang, Y.; Jin, J.; Liu, C.; Jia, P. Indoor 3D Dynamic Reconstruction Fingerprint Matching Algorithm in 5G Ultra-Dense Network. *KSII Trans. Internet Inf. Syst.* **2021**, *15*, 343–364.
22. Fan, J.; Chen, S.; Luo, X.; Zhang, Y.; Li, G.Y. A Machine Learning Approach for Hierarchical Localization Based on Multipath MIMO Fingerprints. *IEEE Commun. Lett.* **2019**, *23*, 1765–1768. [[CrossRef](#)]
23. Zhang, Y.; Wu, C.; Chen, Y. A Low-Overhead Indoor Positioning System Using CSI Fingerprint Based on Transfer Learning. *IEEE Sens. J.* **2021**, *21*, 18156–18165. [[CrossRef](#)]
24. Li, C.; Bast, S.D.; Tanghe, E.; Pollin, S.; Joseph, W. Toward Fine-Grained Indoor Localization Based on Massive MIMO-OFDM System: Experiment and Analysis. *IEEE Sens. J.* **2022**, *22*, 5318–5328. [[CrossRef](#)]
25. Li, Q.; Liao, X.; Liu, M.; Valaee, S. Indoor Localization Based on CSI Fingerprint by Siamese Convolution Neural Network. *IEEE Trans. Veh. Technol.* **2021**, *70*, 12168–12173. [[CrossRef](#)]
26. Sun, X.; Gao, X.; Li, G.Y.; Han, W. Single-Site Localization Based on a New Type of Fingerprint for Massive MIMO-OFDM Systems. *IEEE Trans. Veh. Technol.* **2018**, *67*, 6134–6145. [[CrossRef](#)]
27. Sun, X.; Wu, C.; Gao, X.; Li, G.Y. Fingerprint-Based Localization for Massive MIMO-OFDM System with Deep Convolutional Neural Networks. *IEEE Trans. Veh. Technol.* **2019**, *68*, 10846–10857. [[CrossRef](#)]
28. Wu, C.; Yi, X.; Wang, W.; You, L.; Huang, Q.; Gao, X.; Liu, Q. Learning to Localize: A 3D CNN Approach to User Positioning in Massive MIMO-OFDM Systems. *IEEE Trans. Wirel. Commun.* **2021**, *20*, 4556–4570. [[CrossRef](#)]
29. Pan, C.; Zhou, G.; Zhi, K.; Hong, S.; Wu, T.; Pan, W.; Ren, H.; Renzo, M.D.; Swindlehurst, A.L.; Zhang, R.; et al. An Overview of Signal Processing Techniques for RIS/IRS-Aided Wireless Systems. *IEEE J. Sel. Top. Signal Process.* **2022**, *16*, 883–917. [[CrossRef](#)]
30. Abrardo, A.; Dardari, D.; Renzo, M.D. Intelligent Reflecting Surfaces: Sum-Rate Optimization Based on Statistical Position Information. *IEEE Trans. Commun.* **2021**, *69*, 7121–7136. [[CrossRef](#)]
31. Liu, R.; Wu, Q.; Renzo, M.D.; Yuan, Y. A Path to Smart Radio Environments: An Industrial Viewpoint on Reconfigurable Intelligent Surfaces. *IEEE Wirel. Commun.* **2022**, *29*, 202–208. [[CrossRef](#)]
32. Zhu, J.; Huang, Y.; Wang, J.; Navaie, K.; Huang, W.; Ding, Z. On the Position Optimization of IRS. *IEEE Internet Things J.* **2022**, *9*, 11712–11724. [[CrossRef](#)]
33. Liu, R.; Dou, J.; Li, P.; Wu, J.; Cui, Y. Simulation and Field Trial Results of Reconfigurable Intelligent Surfaces in 5G Networks. *IEEE Access.* **2022**, *10*, 122786–122795. [[CrossRef](#)]
34. Teng, B.; Yuan, X.; Wang, R.; Jin, S. Bayesian User Localization and Tracking for Reconfigurable Intelligent Surface Aided MIMO Systems. *IEEE J. Sel. Top. Signal Process.* **2022**, *16*, 1040–1054. [[CrossRef](#)]
35. Lin, Y.; Jin, S.; Matthaiou, M.; You, X. Channel Estimation and User Localization for IRS-Assisted MIMO-OFDM Systems. *IEEE Trans. Wirel. Commun.* **2022**, *21*, 2320–2335. [[CrossRef](#)]
36. Do, T.N.; Kaddoum, G.; Nguyen, T.L.; Da Costa, D.B.; Haas, Z.J. Multi-RIS-Aided Wireless Systems: Statistical Characterization and Performance Analysis. *IEEE Trans. Commun.* **2021**, *69*, 8641–8658. [[CrossRef](#)]
37. Feng, J.; Zheng, B.; You, C.; Chen, F.; Zhao, S.; Che, W.; Xue, Q. Joint Passive Beamforming and Deployment Design for Dual Distributed-IRS Aided Communication. *IEEE Trans. Veh. Technol.* **2023**, *72*, 13758–13763. [[CrossRef](#)]
38. Huo, Y.; Lin, X.; Di, B.; Zhang, H.; Hernandez, F.J.L.; Tan, A.S.; Mumtaz, S.; Demir, Ö.; Chen-Hu, K. Technology Trends for Massive MIMO towards 6G. *Sensors* **2023**, *23*, 6062. [[CrossRef](#)] [[PubMed](#)]
39. Wang, J.; Tang, W.; Han, Y.; Jin, S.; Li, X.; Wen, C.; Cheng, Q.; Cui, T. Interplay between RIS and AI in Wireless Communications: Fundamentals, Architectures, Applications, and Open Research Problems. *IEEE J. Sel. Areas Commun.* **2021**, *39*, 2271–2288. [[CrossRef](#)]

40. Sagir, B.; Aydin, E.; Ilhan, H. Deep-Learning-Assisted IoT-Based RIS for Cooperative Communications. *IEEE Internet Things J.* **2023**, *10*, 10471–10483. [[CrossRef](#)]
41. Zhong, R.; Liu, X.; Liu, Y.; Chen, Y.; Han, Z. Mobile Reconfigurable Intelligent Surfaces for NOMA Networks: Federated Learning Approaches. *IEEE Trans. Wirel. Commun.* **2022**, *21*, 10020–10034. [[CrossRef](#)]
42. Zhang, H.; Zhang, H.; Di, B.; Bian, K.; Han, Z.; Xu, C.; Zhang, D.; Song, L. RSS Fingerprinting Based Multi-user Outdoor Localization Using Reconfigurable Intelligent Surfaces. In Proceedings of the 2021 15th International Symposium on Medical Information and Communication Technology (ISMICT), Xiamen, China, 14–16 April 2021; pp. 167–172.
43. Liu, R.; Jian, M.; Zhang, W. A TDoA based Positioning Method for Wireless Networks assisted by Passive RIS. In Proceedings of the 2022 IEEE Globecom Workshops (GC Wkshps), Rio de Janeiro, Brazil, 4–8 December 2022; pp. 1531–1536.
44. Dardari, D.; Decarli, N.; Guerra, A.; Guidi, F. LOS/NLOS Near-Field Localization with a Large Reconfigurable Intelligent Surface. *IEEE Trans. Wirel. Commun.* **2022**, *21*, 4282–4294. [[CrossRef](#)]
45. Huang, S.; Wang, B.; Zhao, Y.; Luan, M. Near-Field RSS-Based Localization Algorithms Using Reconfigurable Intelligent Surface. *IEEE Sens. J.* **2022**, *22*, 3493–3505. [[CrossRef](#)]
46. Zhang, H.; Zhang, H.; Di, B.; Bian, K.; Han, Z.; Song, L. MetaLocalization: Reconfigurable Intelligent Surface Aided Multi-User Wireless Indoor Localization. *IEEE Trans. Wirel. Commun.* **2021**, *20*, 7743–7757. [[CrossRef](#)]
47. Brennan, D.G. Linear diversity combining techniques. *Proc. IEEE Inst. Electr. Electron. Eng.* **2003**, *91*, 331–356. [[CrossRef](#)]
48. Yildirim, I.; Uyrus, A.; Basar, E. Modeling and Analysis of Reconfigurable Intelligent Surfaces for Indoor and Outdoor Applications in Future Wireless Networks. *IEEE Trans. Commun.* **2021**, *69*, 1290–1301. [[CrossRef](#)]
49. Zhou, C.; Liu, J.; Sheng, M.; Zheng, Y.; Li, J. Exploiting Fingerprint Correlation for Fingerprint-Based Indoor Localization: A Deep Learning Based Approach. *IEEE Trans. Veh. Technol.* **2021**, *70*, 5762–5774. [[CrossRef](#)]
50. Sinha, R.S.; Hwang, S.H. Improved RSSI-Based Data Augmentation Technique for Fingerprint Indoor Localization. *Electronics* **2020**, *9*, 851–866. [[CrossRef](#)]
51. Wu, S.; Huang, W.; Li, M.; Xu, K. A Novel RSSI Fingerprint Positioning Method Based on Virtual AP and Convolutional Neural Network. *IEEE Sens. J.* **2022**, *22*, 6898–6909. [[CrossRef](#)]

**Disclaimer/Publisher’s Note:** The statements, opinions and data contained in all publications are solely those of the individual author(s) and contributor(s) and not of MDPI and/or the editor(s). MDPI and/or the editor(s) disclaim responsibility for any injury to people or property resulting from any ideas, methods, instructions or products referred to in the content.